



# Fatigue crack growth modeling considering a hybrid propagation strategy

Edmundo R. Sérgio  | Fernando V. Antunes  | Diogo M. Neto 

Department of Mechanical Engineering,  
Centre for Mechanical Engineering,  
Materials and Processes (CEMMPRE),  
University of Coimbra, Coimbra, Portugal

## Correspondence

Edmundo R. Sérgio, Department of  
Mechanical Engineering, Centre for  
Mechanical Engineering, Materials and  
Processes (CEMMPRE), University of  
Coimbra, Coimbra, Portugal.  
Email: [edmundo.sergio@uc.pt](mailto:edmundo.sergio@uc.pt)

## Funding information

This research was funded by the  
Portuguese Foundation for Science and  
Technology (Fundação para a Ciência e a  
Tecnologia [FCT]) under the project with  
reference PTDC/EME-EME/31657/2017  
and by UIDB/00285/2020. The first author  
is also grateful to the FCT for the PhD  
grant with reference 2022.11438.BD.

## Abstract

Fatigue results from the occurrence of several damage mechanisms and their interactions. The cyclic plastic strain and damage accumulation at the crack tip are widely pointed as the main agents behind fatigue crack growth (FCG). In this work, the authors propose the prediction of FCG through a node release numerical model that offers several possibilities regarding the modeling of the mechanisms behind fatigue. A hybrid propagation method is presented where both cumulative plastic strain and porous damage represent parallel propagation criteria. Accordingly, the node is released once either a critical plastic strain or a critical porosity, at the crack tip, is reached. The Gurson–Tvergaard–Needleman (GTN) damage model is employed to predict porous damage evolution through the processes of nucleation and growth of microvoids. The model is validated through comparison with experimental data for the AA2024-T351 aluminum alloy. Finally, the interactions between plastic strain, porous damage, crack closure, and stress triaxiality are accessed.

## KEYWORDS

crack closure, crack tip plastic deformation, fatigue crack growth, GTN damage model

## Highlights

- Fatigue crack growth is numerically predicted considering a hybrid propagation strategy.
- Plastic deformation, in distinct approaches, and porous damage are release criteria.
- Each criterion reflects a perspective of how plastic deformation affects fatigue.
- Porous damage has an increasing effect for higher  $\Delta K$  and stress triaxiality levels.

This is an open access article under the terms of the [Creative Commons Attribution](https://creativecommons.org/licenses/by/4.0/) License, which permits use, distribution and reproduction in any medium, provided the original work is properly cited.

© 2023 The Authors. *Fatigue & Fracture of Engineering Materials & Structures* published by John Wiley & Sons Ltd.

## 1 | INTRODUCTION

Over the decades, fatigue has been one of the most prominent fields of study in mechanical design. The damage tolerance approach is widely used, requiring the ability to predict fatigue crack growth rates (FCGRs). The stress intensity factor,  $K$ , has been for a long time the main parameter regarding fatigue crack growth (FCG). However, its well-known limitations<sup>1</sup> urged the study of the nonlinear crack tip phenomena.<sup>2–7</sup> On previous works, the authors obtained numerical results in good agreement with experimental data, considering the cyclic plastic strain at the crack tip as the fatigue damage main contributor.<sup>8</sup> The numerical model, based on node releases, was firstly developed to predict the plastic Crack Tip Open Displacement (CTOD<sub>p</sub>), which was related with FCGR to produce a crack growth law.<sup>9–13</sup> This parameter proved to be a measure of the crack tip plastic deformation.<sup>14</sup> Additionally, the results shown that crack closure is a fundamental mechanism concerning FCG. Later, the cumulative equivalent plastic strain, at the crack tip, was used as node release criterion, replacing the CTOD<sub>p</sub>.<sup>15,16</sup> In this case, only one  $da/dN$  experimental value is required for calibration, while the CTOD<sub>p</sub> approach needed several values.

Although the cyclic plastic strain at the crack tip is widely accepted as the FCG driving force, this entity may be defined through conceptually distinct conditions, which in turn reflect different mechanisms by which plastic deformation affects the fatigue process. In fact, the crack tip plastic strain may be related with the occurrence of striations on the fracture surfaces, of ductile materials, under cyclic loadings. This phenomenon has been widely analyzed over time<sup>17</sup> and was firstly used to evaluate FCGR through striation spacing and cycle counting.<sup>18</sup> The formation of striations is usually described by Laird's model.<sup>19</sup> Accordingly, the crack tip blunts, during the loading stage, because deformation is highly concentrated at 45°, creating new fracture surfaces. During the unloading phase, compressive stresses reverse the slipping and the crack tip folds into a double notch as the new surface cannot be removed through reconnection of the atomic bonds, in accordance with entropy law.<sup>20</sup> According to this approach, several models correlate the cyclic plastic strain at the crack tip and striation formation to predict FCGR.<sup>5,21–23</sup> Hence, the incremental plastic strain (IPS) criterion was introduced, in the author's numerical model, to predict FCG through the irreversible deformation acting at the crack tip. Accordingly, a node is released when the increment of plastic strain,  $\Delta\epsilon^p$ , reaches a critical value,  $\Delta\epsilon_c^p$ . Therefore, it represents the plastic deformation necessary to the formation of the amount of striations, required to cause a crack growth, over a distance equivalent to the element size. After each propagation,  $\Delta\epsilon^p$  is

set to zero and the preceding plastic deformation only affects the material hardening.

A distinct perspective is followed by assuming the total plastic strain (TPS) approach, which states that the damage accumulation, ahead of the crack tip, is responsible for FCG. In this concept, damage is proportional to cumulative deformation; that is, it considers the accumulation of plastic strain, even when the Gauss points are far from the crack tip, culminating in crack growth when a critical plastic strain,  $\epsilon_c^p$ , is achieved. When a node is released, the value of the cumulative plastic strain,  $\epsilon^p$ , averaged at the Gauss points surrounding the next node, is assumed. The TPS approach is theoretically close to the critical damage models,<sup>24–26</sup> where small volume elements (VEs), often referred as “process zone,”<sup>27</sup> ahead of the crack tip are sequentially fractured once a critical level of damage has accumulated.<sup>28</sup> The FCGR may be either the VE width, considering that the crack breaks a VE each cycle, or the VE width divided by the number of cycles the crack needs to cross it.<sup>29</sup> In the critical damage models, all the damage generated due to the plastic strain ahead of the crack tip is constrained to the VE containing the crack tip. This is, the damage inside the plastic zone, but outside the VE, is small. Thus, a discontinuous crack growth approach is assumed. However, the TPS approach follows Schwalbe's modification of the critical damage models,<sup>30</sup> which recognizes that the strain range in a VE away from the crack tip also causes damage accumulation. This way, the VE at the crack tip is fractured due to the summation of the damage caused by all the load cycles, before and after containing the crack tip.<sup>29</sup> Thus, if the TPS approach is considered, continuous damage begins to accumulate as soon as the material enters the plastic zone.

The numerical model, based on the cumulative plastic deformation at the crack tip, was further improved by considering the nucleation and growth of micro-voids,<sup>31</sup> modeled through the Gurson–Tvergaard–Needleman (GTN) damage model. The porosity was used to account for the material porous damage accumulation, which results in a decrease in material strength and a reduction of the remaining ductility.<sup>32</sup> The FCGR remained controlled by the cumulative equivalent plastic strain at the crack tip. The growth and nucleation of micro-voids was shown to influence  $da/dN$  and crack closure itself, exposing an interdependency of mechanisms at the crack tip. Despite the controversy in this matter,<sup>33</sup> crack closure has been observed experimentally<sup>34–37</sup> and shown to be dominant over residual stresses in the Paris Regime, whereas, in the threshold region, the opposite is expected to occur.<sup>38</sup> The crack closure level was increased by considering growth and nucleation of micro-voids because the porous damage accumulation rises both the size of the plastic zone ahead of the crack tip and the intensity of plastic deformation.<sup>31</sup>

Higher plastic strains increase the plasticity-induced crack closure (PICC),<sup>39</sup> which is one of the main crack closure mechanisms.<sup>40–42</sup> On the other hand, the inclusion of porosity leads to the volumetric expansion of the material, at the crack flanks, promoting the contact between them during unloading. Thus, the modeling of porosity shown to be crucial to understand FCG.

In previous works,  $da/dN$  was evaluated after some crack propagation, as the evolution of the crack closure level and cyclic plastic deformation induced a transient behavior in the  $da/dN$  versus crack length curves,  $da/dN$ - $a$ . However, the GTN application induced a rather adverse effect in the FCGR estimation. Indeed, it causes an amplification of the noise in the propagation curves, due to the occurrence of high porosity levels that destabilize the cyclic plastic strain accumulation. This effect is prevalent for higher values of  $\Delta K$ , due to the highly triaxial stress states that are reached. In fact, the evolution of the porosity defined through the GTN model is highly dependent on the stress triaxiality,<sup>43</sup> which also shown to influence the plastic strain–porosity relation.<sup>44</sup> The GTN formulation, applied by the authors, does not consider any posterior modifications.<sup>45–47</sup> Thus, the evolution of porosity at very low triaxialities, close to zero, is deficient. This is especially relevant because the stress triaxiality is function of the stress state, which is a main parameter within fracture mechanics.<sup>48</sup> However, near the crack tip, high stress triaxialities are expected to occur, making the implemented GTN model very suitable to porosity modeling.

The main objective of this work is to develop hybrid node release strategies, which take into account both the plastic strain and the porous damage at the crack tip. Once applied to the numerical model, these hybrid strategies allow the node release to occur either by reaching a critical cumulative cyclic plastic strain or a critical porosity,  $f_c$ . The numerical predictions of FCGR are compared with experimental measurements, using  $da/dN$ - $\Delta K$  curves, in order to access the accuracy of the proposed hybrid strategies for node release. Besides, as previous works<sup>31</sup> suggested a close relation between plastic strain, porosity, stress triaxiality, crack closure, and  $\Delta K$ , the study of the interactions between these parameters is also contemplated here.

The structure of the paper is as follows: The material model is described in Section 2.1, and then the employed geometry, mesh, and loading case are discussed in Section 2.2. The crack propagation algorithm together with the distinct node release criteria, including the hybrid propagation strategies, are depicted in Section 2.3. The hybrid FCG propagation histories are discussed in Section 3.1. Stress triaxiality,  $\Delta K$ , and porous damage are firstly related in Section 3.2, as they directly influence the propagation history. Section 3.3 contains the comparison between numerical FCGRs and the experimental

data. Plastic strain and crack closure are then introduced in Section 4. Moreover, the discussion section contains the mapping of porosity and plastic strain, which are field variables, ahead of the crack tip. Stress triaxiality and crack closure are also evaluated. These are the main mechanisms considered by the employed model.

## 2 | NUMERICAL MODEL

This study considers the 2024-T351 aluminum alloy, which is used in several engineering applications due to its high strength to weight ratio. All the numerical simulations were conducted in the in-house finite element code DD3IMP,<sup>49,50</sup> which uses an updated Lagrangian scheme to describe the evolution of the deformation process. The mechanical model assumes the elastic strains to be negligibly small with respect to unity and considers large elastoplastic strains and rotations.

### 2.1 | Material constitutive model

A phenomenological elastic–plastic constitutive model was used to describe the behavior of the Al2024-T351 alloy. The elastic behavior is modeled through Hooke's law, considering a dependency of the Young modulus on the porosity:

$$E = (1 - f) \cdot E_0, \quad (1)$$

where  $E_0$  is the material Young modulus and  $E$  is the effective modulus, which will be applied in the elastoplastic constitutive calculations. The matrix is modeled by the von Mises yield criterion, where the equivalent stress ( $\bar{\sigma}$ ) is given by Equation (2), under an associated flow rule.

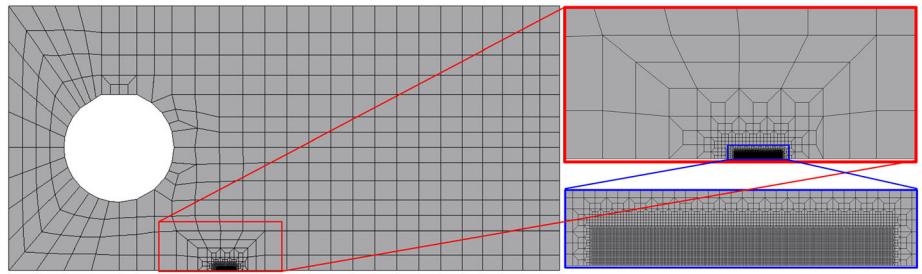
$$\bar{\sigma} = \sqrt{\frac{3}{2} \boldsymbol{\sigma}' : \boldsymbol{\sigma}'}, \quad (2)$$

where  $\boldsymbol{\sigma}'$  is the deviatoric stress tensor. Due to cyclic loading, the material ahead of a crack tip experiences complex states of deformation involving both tension and compression stresses, which are induced by the loading and unloading phases, respectively.<sup>51</sup> The material hardening (or softening, depending on the dislocation substructures<sup>52</sup>) under cyclic loading is supposed to be steady after a certain number of cycles.<sup>53</sup> Consequentially, there is a stabilization of the yield surface, which can be modeled by adding an isotropic component to the flow stress.<sup>52</sup> The Swift isotropic hardening law, Equation (3), was chosen to embody this characteristic on the evolution of the yield surface.





**FIGURE 2** Finite element mesh. The refined zones are shown in the image on the bottom right corner. [Colour figure can be viewed at [wileyonlinelibrary.com](http://wileyonlinelibrary.com)]



study, since the experimental results were obtained in CT specimens with a thickness of 12 mm, where plain strain state is expected to be dominant. This is, since the surface zone represents a minor fraction of the specimen, the plane stress condition that occurs here should not influence the global fatigue behavior.

The specimen was discretized with 7287, 4-node, plane strain finite elements and 7459 nodes (see Figure 2). The region surrounding the crack growth path is meshed with elements of 8  $\mu\text{m}$  element size, which allow to accurately evaluate the strong gradients of stresses and strains at this zone.<sup>65</sup> To reduce the computational cost, the outer region was defined by a coarser mesh.

### 2.3 | Crack propagation algorithm

The FCG process is modeled using a node release strategy with several release criteria. The FCGR is obtained from the ratio between the crack increment, 8  $\mu\text{m}$ , which is the element size, and the number of load cycles,  $\Delta N$ , required to achieve the node release criterion (Equation 7).

$$\frac{da}{dN} = \frac{8}{\Delta N}. \quad (7)$$

This work considers five different approaches for the node release strategy:

- A. TPS approach neglecting the porous damage in the evaluation of the plastic strain: TPS (no porous damage);
- B. TPS approach considering the GTN model in the evaluation of the plastic strain: TPS;
- C. IPS approach considering the GTN model in the evaluation of the plastic strain: IPS;
- D. TPS approach combined with porous damage caused node releases (hybrid): TPS + damage release (hybrid TPS); and
- E. IPS approach combined with porous damage caused node releases (hybrid): IPS + damage release (hybrid IPS).

The first three methods consider the cumulative plastic strain at the crack tip, as single criterion for node release. This way, the release occurs when reached either the critical plastic strain,  $\epsilon_c^p$ , if the TPS approach is followed (Models A and B) or the critical increment of plastic strain,  $\Delta\epsilon_c^p$ , if IPS is considered (Model C). Model A differs from Model B due to the absence of the GTN model. Note that, due to the singularity induced by the geometrical discontinuity of the crack,<sup>30</sup> the plastic deformation at the node containing crack tip is computed through the average of the value at the two surrounding Gauss points. Hybrid propagation methods are also presented, where cumulative cyclic plastic strain and porous damage represent parallel propagation criteria. Accordingly, the node is released once either criterion is reached (Models D and E). Note that IPS and TPS approaches are still distinguished, regarding the cyclic plastic strain release criterion. The assessment of  $da/dN$  is made only through the propagations caused by reaching the critical cyclic plastic strain. This is because reaching  $f_c$  physically means that the small region of material ahead of the crack tip has accumulated all the porous damage the material can support. In other words, the material, which has a void volume fraction of  $f_c$ , has no longer the sufficient mechanical resistance to support the applied load. Thus, the crack is supposed to propagate until it reaches a less damaged material. However, the dimension of the critically damaged material is expected to be much lesser than the element size. Also, as no coalescence criterion is applied, the modeling of porosity is not sufficiently precise to allow the evaluation of  $da/dN$  through porous damage propagations. Note that, due to the nature of porous damage, the critical porosity is evaluated in a similar way as  $\epsilon_c^p$  in the TPS approach. This is, once a node release occurs, the porosity computed at the Gauss points adjacent to the crack tip is assumed and a porous damage release occurs when the absolute porosity reaches the critical value,  $f_c$ .

Since the FCGR is usually low ( $<1 \mu\text{m}/\text{cycle}$ ), the numerical analysis of the crack growth is simplified by considering different sizes for the initial straight crack, which allows to evaluate a relatively wide range of  $\Delta K$  values with the same loading case. Accordingly, the

initial crack sizes,  $a_0$ , considered in the numerical analysis are 11.5, 14, 16.5, 19, and 21.5 mm. Note that  $\Delta K$  is used only to present and compare results, since it is never used in the numerical model it is not necessary to assess the small-scale yielding (SSY) condition. Even though the  $\Delta K$  approach has the aforementioned limitations, it represents a suitable and familiar way to express and compare results within the Paris Regime. For each crack length, the FCG is evaluated only after some crack propagations to stabilize the cyclic plastic deformation and the crack closure level. Finally, the contact between the crack flanks is modeled considering a rigid plane surface aligned with the crack symmetry plane, allowing to precisely model PICC.<sup>66</sup>

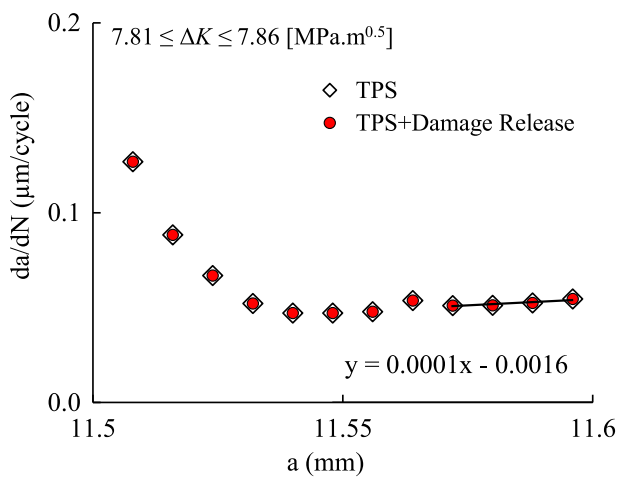


FIGURE 3 Predicted  $da/dN$  as a function of the crack length for  $a_0 = 11.5$  mm. TPS, total plastic strain [Colour figure can be viewed at [wileyonlinelibrary.com](https://onlinelibrary.wiley.com/doi/10.1111/ffe.13950)]

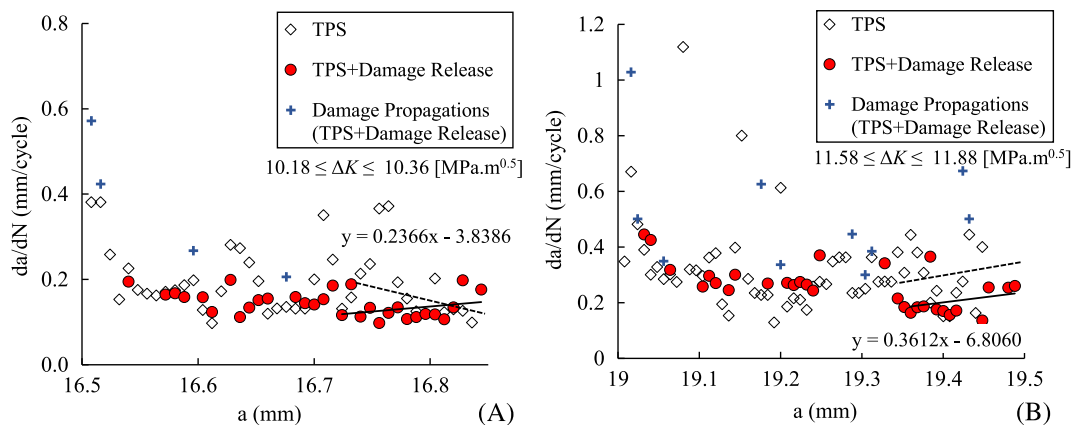


FIGURE 4 Propagation history,  $da/dN$ - $a$ , for (A)  $a_0 = 16.5$  mm and (B)  $a_0 = 19$  mm. Note that the trend lines consider only the final points of the curve, in order to refer to the stable crack growth zone. TPS, total plastic strain [Colour figure can be viewed at [wileyonlinelibrary.com](https://onlinelibrary.wiley.com/doi/10.1111/ffe.13950)]

## 3 | RESULTS

### 3.1 | Fatigue crack growth rate

Figure 3 presents the  $da/dN$  as a function of the crack size,  $a$ , for an initial crack size,  $a_0 = 11.5$  mm, comparing the TPS and TPS + damage release criteria. This initial crack size, considering  $R = 0.1$ , results in a  $\Delta K$  variation between 7.8 and 7.9  $\text{MPa}\cdot\text{m}^{0.5}$ . For these  $\Delta K$  values, no damage propagations occur. Thus, both hybrid TPS and TPS criteria lead to a similar crack growth rate. The  $da/dN$  is higher at the first propagations because the material is virgin, concerning plastic deformation, and crack closure has not built up yet. Once this occurs, there is a stabilization of  $da/dN$ , allowing a correct assessment of the FCGR. Note that the same findings and conclusions were reached comparing the IPS and IPS + damage release criteria.

Figure 3 shows that for smaller  $\Delta K$  values, porous damage has a minor impact and either considering or not considering the damage-based release criterion leads to similar results. The  $da/dN$ - $a$  curves, for higher initial crack sizes, are presented in Figure 4A for  $a_0 = 16.5$  mm and in Figure 4B for  $a_0 = 19$  mm. Note that the variation ranges of  $\Delta K$ , induced by the variation of  $a$  due to successive propagations, are depicted in each figure. Results show that porous damage propagations, which are separated from the plastic strain propagations in the hybrid criterion, increase with  $a_0$ . Not all the porous damage propagations are presented, because of the scale adopted for the figures. In both considered initial crack sizes, the first two node releases are caused by porous damage. Thus, in a virgin material and in the lack of crack closure, the porous damage build-up is faster than the plastic strain evolution. When the  $da/dN$  starts to stabilize,

propagations vary between porous damage caused and plastic strain caused. In both cases, the  $da/dN$  evaluation is simple, the porous damage caused propagations are neglected, and a trend line is added to the final plastic strain propagations. Then,  $da/dN$  is computed from the respective fitted equation, at the last recorded crack size. The trend line is added to the final points, while the number of considered points is the largest that still provides a positive slope curve. In fact, considering all the data would cause a negative slope function, due to the importance of the first propagations. However, after the stabilization of crack closure and plastic zones, the FCGR should start to increase, as higher crack sizes and consequently  $\Delta K$  values are achieved. Trend lines, plotted with dotted stripes, were also added to the TPS criterion, in both figures, and differ largely from the ones obtained with the hybrid strategy.

The results presented in Figure 4 show that, for higher  $\Delta K$  values, the porous damage acquires a critical effect on FCG. Indeed, the occasional accumulation of high levels of porosity leads to a drop in the material load-carrying capacity. This destabilizes the plastic strain modeling, causing significant oscillations in the required load cycles to a crack propagation, and this way in  $da/dN$ , which induces an undefined behavior in the propagation curves. The dispersion in the node release occurrences, over the crack growth considering IPS and TPS criteria, prompted the introduction of the porous damage-based release criterion. In fact, at higher crack sizes, the severe oscillations required the disposal of certain data points, which were too far away from acceptable values, to achieve a smoother propagation allowing the  $da/dN$  evaluation. The introduction of porous damage propagations stabilized the crack tip plastic strain-based node releases. This way, by considering only the plastic strain-related criterion for  $da/dN$  evaluation, the FCGR may be calculated without neglecting any point.

### 3.2 | Stress triaxiality effect

The higher amount of porous damage propagations in Figure 4B indicates that, as expected, higher values of  $\Delta K$  are related to higher incidences of micro-voids. However, as referred before, the evolution of porosity is highly dependent of the stress triaxiality at the crack tip, which is related to  $\Delta K$  itself. It is important to separate the effects of  $\Delta K$  and stress triaxiality because the latter is very dependent of the dominant stress state at the crack tip. Thus, for similar  $\Delta K$  values, distinct stress triaxialities may be obtained depending on the thickness, geometry, and crack length. While this work is focused on plane strain conditions, this detail is important in real

application conditions. This way, to obtain a clear picture of the influence of stress triaxiality, in the amount of porous damage propagations, both entities were related in Figure 5. The stress triaxiality was measured at the crack tip, in the instant of maximum force in each load cycle, through Equation (8), and then averaged for all the load cycles.

$$T = \frac{p}{\bar{\sigma}} = \frac{\frac{\sigma_{xx} + \sigma_{yy} + \sigma_{zz}}{3}}{\sqrt{\frac{1}{2}[(\sigma_{xx} - \sigma_{yy})^2 + (\sigma_{yy} - \sigma_{zz})^2 + (\sigma_{zz} - \sigma_{xx})^2 + 3(\sigma_{xy}^2 + \sigma_{xz}^2 + \sigma_{yz}^2)]}} \quad (8)$$

The amount of propagations due to porous damage is presented as a percentage of the total number of propagations. Approximate  $\Delta K$  levels were added to allow a simpler comparison between results. In concordance with Figure 3, no porous damage propagations occur for  $\Delta K \approx 7.8 \text{ MPa}\cdot\text{m}^{0.5}$ , despite the relatively high value of the stress triaxiality. Thus, at this  $\Delta K$ , plastic strain dominates over porosity and stress triaxiality assumes a secondary role. The percentage of porous damage propagations starts to increase with  $\Delta K$ , as well as the stress triaxiality. Micro-voids effect only gets predominant for the two higher initial crack sizes, namely,  $a_0 = 19 \text{ mm}$  and  $a_0 = 21.5 \text{ mm}$ . This way, Figure 4A refers to a cyclic plastic strain dominant propagation history and Figure 4B to a porous damage predominant sequence of node releases.

Different propagation strategies induce different stress triaxialities for similar  $\Delta K$  values. For  $a_0 = 16.5$ ,

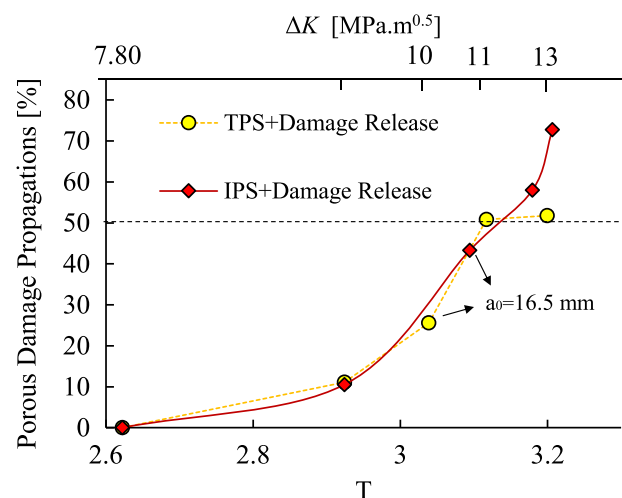


FIGURE 5 Percentage of porous damage propagations in terms of the stress triaxiality at the crack tip. IPS, incremental plastic strain; TPS, total plastic strain [Colour figure can be viewed at [wileyonlinelibrary.com](http://wileyonlinelibrary.com)]

the hybrid IPS strategy houses a higher stress triaxiality and consequentially more porous damage propagations than the hybrid TPS criterion. Indeed, in the IPS criteria, the percentage of porous damage propagations rises very quickly with stress triaxiality. However, the two higher initial crack sizes, though representing very distinct  $\Delta K$  values, have similar stress triaxialities. This way, with the increase in  $\Delta K$ , an increment in this parameter leads to smaller and smaller increases on the stress triaxiality. Even so, the higher  $\Delta K$  value has a percentage of nearly 80% of damage propagations, thus, here, the regime is rather closer to the ductile fracture than to the Paris Regime.

In the hybrid TPS strategy, there is a stagnation in the percentage of damage propagations above  $\Delta K = 11 \text{ MPa}\cdot\text{m}^{0.5}$ . This percentage seats near 50%; thus, porous damage never gets completely dominant over plastic strain, despite the very distinct  $\Delta K$  levels and stress triaxialities. This occurs because, in the hybrid TPS strategy, both criteria are conceptually close to the critical damage models. Consequently, the crack tip damage is divided by the plastic strain and porous damage. Additionally, the TPS strategy requires an absolute smaller plastic strain level ahead of the crack tip, easing this kind of propagation. This last detail will be explored later in this study.

### 3.3 | Hybrid propagation results

The damage tolerance approach requires the calculation of  $da/dN$ , which is the basic outcome of any FCG study. Usually, this result is presented in terms of  $\Delta K$ ; therefore, the same approach is here followed. As the applied model makes use of release criteria, the position of the

numerical curves is function of the values adopted for  $\Delta\varepsilon_c^p$ ,  $\varepsilon_c^p$ , and  $f_c$ , while the slope remains constant. This way, a calibration process is required to correctly position the numerical curves. This is achieved by changing the values of  $\Delta\varepsilon_c^p$ ,  $\varepsilon_c^p$ , and  $f_c$  until the middle point of the numerical curve overlaps the experimental results. The calibration process provided a critical plastic strain,  $\varepsilon_c^p = 270\%$ , a critical increment of plastic strain,  $\Delta\varepsilon_c^p = 270\%$ , and a critical porous damage,  $f_c = 10\%$ . These values are supposed to be material properties and should provide results in agreement with experimental data for distinct stress ratios.

The  $da/dN$ - $\Delta K$  results for  $R = 0.1$  are presented in Figure 6A, whereas Figure 6B shows the curve for  $R = 0.5$ . Each presented point represents a distinct initial crack size. Note that the minimum  $\Delta K$ , depicted in each figure, was defined numerically while the maximum comes from the experimental test. For the smaller stress ratio, the numerical results are very close to the experimental ones, especially in the case of the hybrid IPS approach. In fact, while for the smaller  $\Delta K$  values, both strategies provide coincident results, they start to diverge once higher crack sizes are reached. This occurs because, in the hybrid IPS approach, plastic strain propagations occur when  $\Delta\varepsilon_c^p$  is reached. This way, if plastic deformation has already occurred in a node, before it contains the crack tip, on its release, the total deformation will be the sum of the initial deformation plus  $\Delta\varepsilon_c^p$ . In the hybrid TPS case, plastic strain never surpasses  $\varepsilon_c^p$ . This way, since both release criteria take the same value ( $\Delta\varepsilon_c^p = \varepsilon_c^p$ ), higher plastic strains need to be reached, in the hybrid IPS approach, for propagation to occur, resulting in a  $da/dN$  slow down. This is evidenced by the trend lines, in the right corner, which clearly show that the hybrid IPS and experimental lines have a very similar slope. Note

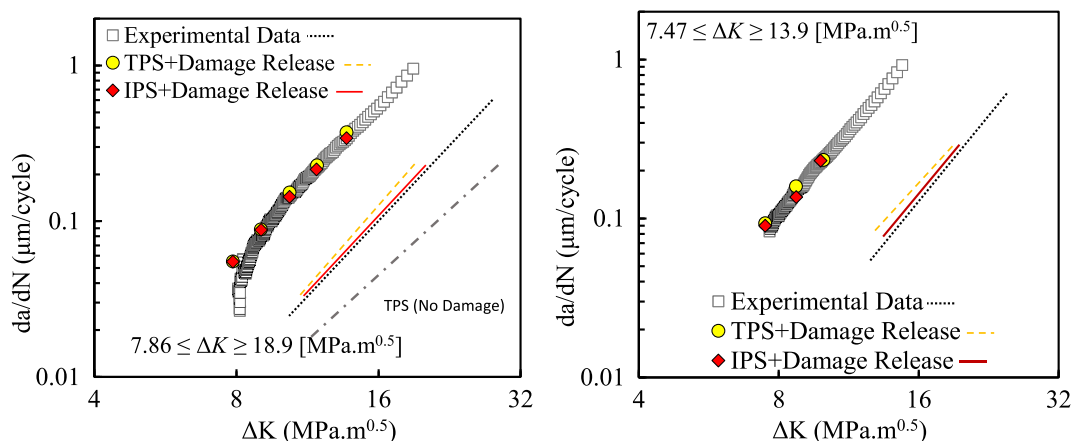


FIGURE 6  $da/dN$ - $\Delta K$  curves, considering  $\Delta\varepsilon_c^p = 270\%$ ,  $\varepsilon_c^p = 270\%$ , and  $f_c = 10\%$ , for (A)  $R = 0.1$  and (B)  $R = 0.5$ . The experimental results come from reference.<sup>19</sup> IPS, incremental plastic strain; TPS, total plastic strain [Colour figure can be viewed at [wileyonlinelibrary.com](https://onlinelibrary.wiley.com/terms-and-conditions)]



that these trend lines have been transferred to near the right bottom corner to ease its visualization; therefore, one should only look to their slope.

The upper part of the experimental data is not modeled because both strategies provide a behavior rather closer to ductile fracture, resulting in propagations almost every cycle and severe convergence problems. Accordingly, the experimental data also present a smaller density of points on that zone, suggesting that fracture is very close. Note that an additional trend line is displayed. It refers to the  $da/dN-\Delta K$  results obtained with the TPS (no damage) version. It was added to highlight the importance of the porous damage consideration, as its slope differs greatly from experimental results. In the case of  $R = 0.5$ , the numerical data also closely follow experimental results. However, the ductile fracture behavior is reached earlier, preventing the modeling of a wider range of  $\Delta K$  values. Although the promising results, the inability to predict FCG for the upper part of the Paris Regime, for this stress ratio, requires further study. This was the main reason behind the focus on  $R = 0.1$  results on the previous discussions.

## 4 | DISCUSSION

The FCG phenomenon results from the interaction of several mechanisms at the crack tip zone. Additionally, in the Paris Regime, previous results<sup>15,44,67</sup> pointed out crack closure and porous damage as the main actors in terms of mechanisms. Thus, the propagation histories presented earlier may be explained through the analysis of the strain and porosity fields, jointly with the assessment of stress triaxiality and crack closure, which is evaluated through Equation (9).

$$U^* = \frac{F_{\text{open}} - F_{\text{min}}}{F_{\text{max}} - F_{\text{min}}}, \quad (9)$$

where  $F_{\text{open}}$  is the crack opening load. This parameter quantifies the percentage of the load cycle during which the crack is closed.

Since porosity and plastic strain are field variables, they were mapped in the stable  $da/dN$  zone, for the different initial crack sizes and propagation strategies presented above. This is achieved by plotting lines that connect the points with the same properties, that is, iso-lines. Figure 7 presents the obtained results for  $a_0 = 11.5$  mm, namely, TPS strategy in Figure 7A and hybrid TPS in Figure 7B. The chosen load cycles refer to equivalent  $\Delta K$  levels, guarantying comparability. For smaller  $\Delta K$  values, IPS and TPS strategies, as well as their hybrid variants, are identical. Therefore, similar maps are expected and, consequently, the hybrid IPS is not presented. Indeed, the results show that, due to the concordance of hybrid TPS and TPS strategies presented in Figure 3, the porosity and strain distributions ahead of the crack tip are similar. Moreover, the plastic zone size and stress triaxiality are the same with the only difference occurring in the crack closure level. However, this difference is very small, not causing differences in the remaining results. Note that both porosity and plastic strain have similar distributions, which indicates a relation between them. Thus, the propagation results (Figure 3) are fully explained. On the other hand, the presented stress triaxialities are not in accordance with the ones presented in Figure 5. This occurs because those results refer to the average of all the propagations. During each propagation, this entity tends to decrease with the accumulation of load cycles, especially for smaller  $\Delta K$  levels, explaining the obtained stress triaxialities.

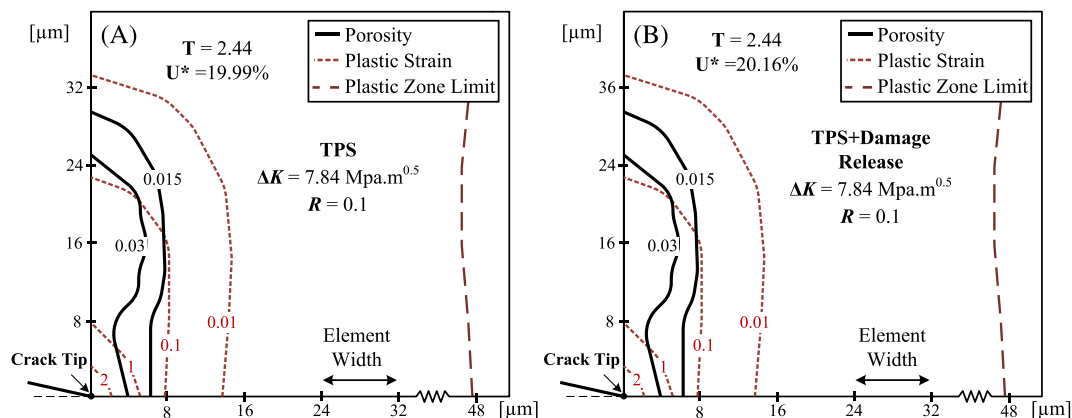
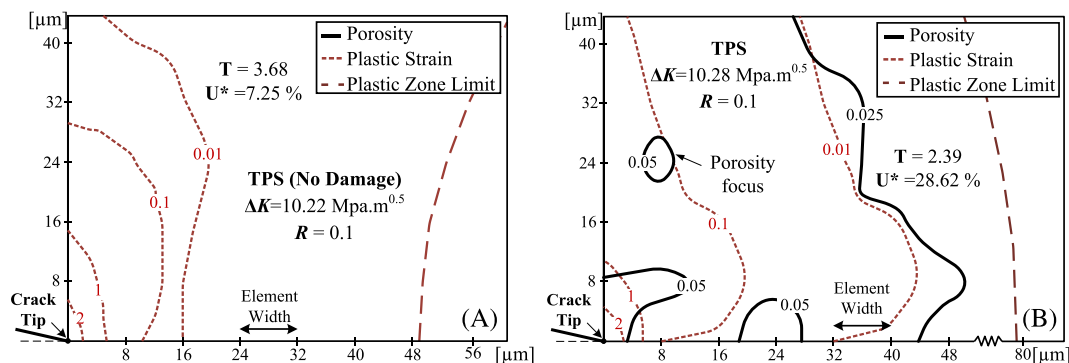
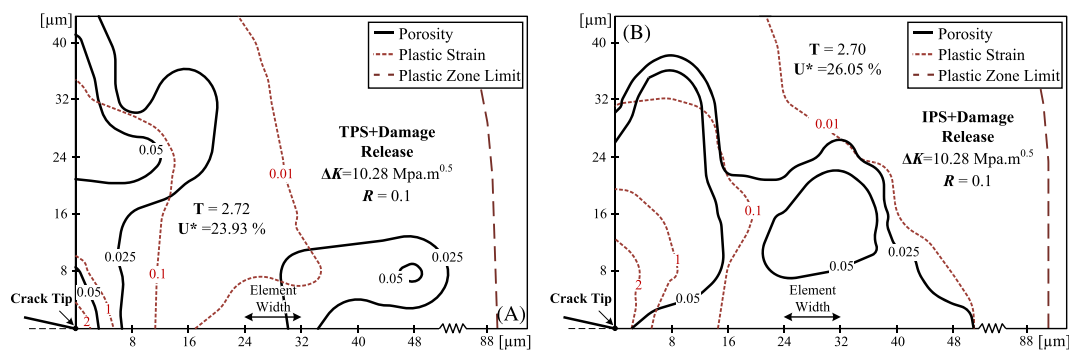


FIGURE 7 Iso-lines map of the porosity and plastic strain ahead of the crack tip at  $a = 11.564$  mm, that is, after 8 propagations, for (A) TPS strategy and (B) TPS + damage release (hybrid TPS) strategy. The stress triaxiality and crack closure levels are presented. TPS, total plastic strain [Colour figure can be viewed at [wileyonlinelibrary.com](http://wileyonlinelibrary.com)]



**FIGURE 8** Iso-lines map of the porosity and plastic strain ahead of the crack tip for (A) TPS without damage modeling after 10 propagations and (B) TPS with GTN but no damage release after 25 propagations. Comparison was not made at the same  $\Delta K$  because  $da/dN$  is much smaller without damage and the crack tip has not grown enough to allow it. TPS, total plastic strain [Colour figure can be viewed at [wileyonlinelibrary.com](http://wileyonlinelibrary.com)]



**FIGURE 9** Iso-lines map for (A) TPS + damage release after 25 propagations and (B) hybrid IPS after 25 propagations. IPS, incremental plastic strain; TPS, total plastic strain [Colour figure can be viewed at [wileyonlinelibrary.com](http://wileyonlinelibrary.com)]

The intrinsic relation between porosity and plastic strain is evidenced by the results presented in Figure 8A,B, which both consider the TPS strategy for  $a_0 = 16.5$  mm. Accordingly, Figure 8A presents the map for FCG modeling without considering porosity. Figure 8B shows the same results, with GTN, but without porous damage releases. Here, the plastic strain distributions differ greatly. Without porous damage, the plastic strain field is like the ones obtained in Figure 7, for a smaller  $\Delta K$ . On the other hand, Figure 8B shows that the plastic strain field is strongly affected by the porous damage. Besides, the plastic zone size is also larger considering micro-voids. Thus, the plastic strain affects porous damage, and vice versa. Nevertheless, for smaller  $\Delta K$  levels, the porosity influence is minor.

The stress triaxiality and crack closure are also affected by the porous damage inclusion. Accordingly, stress triaxiality drops, which occurs because porosity accommodates volumetric changes, which otherwise would manifest as hydrostatic pressure. Crack closure rises because the plastic strain intensity and plastic zone

size also rise, increasing PICC. Besides, with porosity, the volume of the plastically deformed material in the crack flanks increases, promoting the contact between them.

There are dispersed points where porosity evolution is focused (see Figure 8B). This occurs due to a numerical tolerance effect. The computed mean stress presents some local discrepancies, due to the residual tolerance associated with numeric methods. This causes a higher rise in porosity in those points, which affects the stress state, ending up to eventually increase porosity in a chain effect. This is also to blame for the oscillations verified in propagations without porous damage release. Concretely, the porosity focus points end up accumulating unrealistic huge amounts of damage, leading to stress concentrations away from the crack tip.

The damage propagations smooth the noise in the propagation history because they prevent the unrealistic damage accumulation, in porosity focus points, retaining the major stress concentration at the crack tip. As referred, the effect of porosity is enlarged for higher  $\Delta K$  levels. Thus, with the increase of the initial crack size,

the maps regarding distinct release criteria are supposed to diverge further, as pointed out in the discussion of Figure 4. This hypothesis is verified by comparing Figure 8A with Figure 9A, which presents the results for  $a_0 = 16.5$  mm but considering the hybrid TPS approach. Despite the high porous damage in the area ahead of the crack tip, the 0.025% void volume fraction iso-line shows that porous damage is contained in smaller areas than in the TPS approach.

The application of the hybrid TPS approach yields different values for the stress triaxiality and crack closure. The smaller damaged area in the hybrid criterion results in lower stress triaxiality and crack closure levels. On the other hand, the plastic zone size is larger due to a porosity focus point, which still occurs considering porous damage releases, that pushes the plastic zone further.

To clarify the  $da/dN$  difference in the hybrid IPS and hybrid TPS approaches, Figure 9B presents the map for IPS + damage release criterion. Again, here, the higher damaged area results in a lower stress triaxiality and crack closure level. This is crucial, because crack closure tends to protect the material at the crack tip, reducing the effective stress intensity, explaining the lower  $da/dN$  obtained for the hybrid IPS approach. On the other hand, the hybrid IPS porous damage is more intense and spreads over a larger area. This occurs because the level of plastic strain is higher.

The hybrid IPS strategy is the one that best translates the physical process of FCG. In addition to providing the results closest to the experimental ones, previous works have verified the coexistence of fatigue striations and micro-voids in a fatigue propagation zone. Accordingly, Borrego et al.<sup>68</sup> observed widely dispersed micro-void formation around second-phase particles in the fracture region of an AlMgSi1-T6 alloy, containing fairly well-

formed fatigue striations, as shown in Figure 10. Using the IPS strategy, the plastic strain-related node releases are responsible for modeling the FCG process by cyclic striations, while the GTN model predicts the influence of neighboring micro-voids. Therefore, these two mechanisms are modeled in the present study, in a coupled way.

Some limitations to the model can still be pointed out. Accordingly, in the current form, no porosity evolution is predicted both under pure shear stress states and low stress triaxialities ( $-1/3 \leq T \leq 1/3$ ). Even if, in these conditions, the void volume fraction does not increase, void distortion and inter-void linking contribute to material softening and constitute an effective increase in damage. This shortcoming of GTN may be rectified through the Nahshon and Hutchinson modification,<sup>45</sup> which introduces an effective void volume fraction that accounts for the effects of void deformation and reorientation. Additionally, the adopted GTN model predicts only the growth and nucleation of micro-voids. This is a consequence of the formulation of the initial Gurson model, which only considers a homogenous deformation.<sup>69</sup> However, coalescence is suggested as an important mechanism in FCG, controlling the  $K_{max}$  effect,<sup>70</sup> and consequentially also the stress ratio effect. This void evolution stage is also expected to affect the evaluation of  $da/dN$  using the porous damage propagations. Thus, a physical-based coalescence criterion, like Thomason's plastic limit load model,<sup>63</sup> is of first order to completely describe the material degradation and rupture due to micro-void damage.

## 5 | CONCLUSIONS

In this study, FCG is numerically predicted considering a hybrid propagation strategy. Both cyclic plastic deformation and porous damage act as parallel release criteria. Two different approaches are compared. The hybrid IPS strategy considers that the cyclic plastic strain is responsible for FCG due to striation forming, while porosity accounts for the effects of micro-voids occurrence and evolution. On the other hand, the hybrid TPS criterion considers the plastic strain as a crack tip damage mechanism; thus, both node release options are related to a critical damage perspective of fatigue. The main conclusions are as follows:

- Both hybrid IPS and hybrid TPS approaches differ only for higher  $\Delta K$  levels.
- The IPS strategy provides results, closer to the experimental ones, for both stress ratios ( $R = 0.1$  and  $R = 0.5$ ).

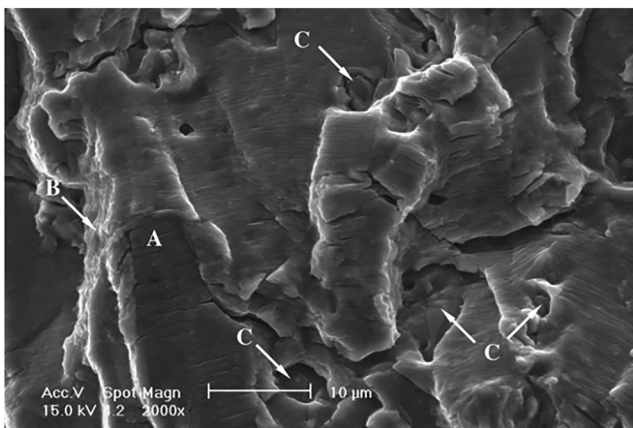


FIGURE 10 Scanning electron microscope images of fracture surfaces in the AlMgSi1-T6.<sup>68</sup> The second-phase particles are labeled C, while the fatigue striations are labeled A.

- The upper part of the  $da/dN$ - $\Delta K$  curves is hard to predict. The model presents a behavior closer to ductile fracture, due to the approximation to the accelerated FCG regime and therefore the fracture toughness of the material.
- The porous damage has an increasing effect for higher  $\Delta K$  values and affects the plastic deformation distribution ahead of the crack tip, as well as the stress triaxiality and crack closure levels, decreasing the first and rising the second.
- Stress triaxiality and  $\Delta K$  control the amount of damage propagations. Accordingly, higher fractions of porous damage propagations occur for higher  $\Delta K$  and stress triaxiality levels.
- In the lower region of the Paris Regime, the damage propagations are almost inexistent, while they are dominant at the region closer to ductile fracture.

### CONFLICT OF INTEREST

The authors declare no conflict of interest.

### AUTHOR CONTRIBUTIONS

**Fernando V. Antunes:** conceptualization. **Edmundo R. Sérgio:** methodology. **Diogo M. Neto:** software. **Edmundo R. Sérgio:** formal analysis. **Edmundo R. Sérgio, Fernando V. Antunes, and Diogo M. Neto:** writing—original draft preparation. **Edmundo R. Sérgio, Fernando V. Antunes, and Diogo M. Neto:** writing—review and editing. All authors have read and agreed to the published version of the manuscript.

### DATA AVAILABILITY STATEMENT

The data that support the findings of this study are available from the corresponding author upon reasonable request.

### ORCID

Edmundo R. Sérgio  <https://orcid.org/0000-0001-6256-2509>

Fernando V. Antunes  <https://orcid.org/0000-0002-0336-4729>

Diogo M. Neto  <https://orcid.org/0000-0002-2296-4009>

### REFERENCES

1. Kfoury AP. Limitations on the use of the stress intensity factor,  $k$ , as a fracture parameter in the fatigue propagation of short cracks. *Fatigue Fract Eng Mater Struct*. 1997;20:1687-1698.
2. Pommier S, Hamam R. Incremental model for fatigue crack growth based on a displacement partitioning hypothesis of mode I elastic-plastic displacement fields. *Fatigue Fract Eng Mater Struct*. 2007;30:582-598.
3. Tong J, Zhao LG, Lin B. Ratchetting strain as a driving force for fatigue crack growth. *Int J Fatigue*. 2013;46:49-57.
4. Bodner SR, Davidson DL, Lankford J. A description of fatigue crack growth in terms of plastic work. *Eng Fract Mech*. 1983;17(2):189-191.
5. Pelloux RMN. Crack extension by alternating shear. *Eng Fract Mech*. 1970;1(4):697-704.
6. Gu I, Ritchie RO. On the crack-tip blunting model for fatigue crack propagation in ductile materials. In: Panontin TL, Sheppard SD, eds. *Fatigue and Fracture Mechanics: 29th Volume*. West Conshohocken, PA: ASTM International; 1999: 552-564.
7. Wang W, Hsu CTT. Fatigue crack growth rate of metal by plastic energy damage accumulation theory. *J Eng Mech*. 1994;120(4):776-795.
8. Jiang Y, Feng M. Modeling of fatigue crack propagation. *J Eng Mater Technol Asme - J ENG MATER TECHNOL*. 2004;126(1): 77-86.
9. Antunes FV, Branco R, Prates PA, Borrego L. Fatigue crack growth modelling based on CTOD for the 7050-T6 alloy. *Fatigue Fract Eng Mater Struct*. 2017;40(8):1309-1320.
10. Antunes FV, Serrano S, Branco R, Prates P. Fatigue crack growth in the 2050-T8 aluminium alloy. *Int J Fatigue*. 2018;115: 79-88.
11. Antunes FV, Ferreira MSC, Branco R, Prates P, Gardin C, Sarrazin-Baudoux C. Fatigue crack growth versus plastic CTOD in the 304L stainless steel. *Eng Fract Mech*. 2019;214: 487-503.
12. Prates P, Marques A, Borges M, Branco R, Antunes FV. Numerical study on the variability of plastic CTOD. *Materials (Basel)*. 2020;13(6):1276.
13. Borges M, Lopez-Crespo P, Antunes FV, et al. Fatigue crack propagation analysis in 2024-T351 aluminium alloy using non-linear parameters. *Int J Fatigue*. 2021;153:106478.
14. Vasco-Olmo J, Diaz Garrido F, Antunes FV, James M. Plastic CTOD as fatigue crack growth characterising parameter in 2024-T3 and 7050-T6 aluminium alloys using DIC. *Fatigue Fract Eng Mater Struct*. 2020;43(8):1719-1730.
15. Borges M, Neto DM, Antunes FV. Numerical simulation of fatigue crack growth based on accumulated plastic strain. *Theor Appl Fract Mech*. 2020;108:102676.
16. Ferreira FF, Neto DM, Jesus JS, Prates PA, Antunes FV. Numerical prediction of the fatigue crack growth rate in SLM Ti-6Al-4V based on crack tip plastic strain. *Metals (Basel)*. 2020;10.
17. Lynch S. Some fractographic contributions to understanding fatigue crack growth. *Int J Fatigue*. 2017;104:12-26.
18. Sunder R, Seetharam SA, Bhaskaran TA. Cycle counting for fatigue crack growth analysis. *Int J Fatigue*. 1984;6(3):147-156.
19. Laird C, Smith GC. Crack propagation in high stress fatigue. *Philos Mag a J Theor Exp Appl Phys*. 1962;7(77):847-857.
20. Levkovitch V, Sievert R, Svendsen B. Simulation of fatigue crack propagation in ductile metals by blunting and re-sharpening. *Int J Fract*. 2005;136(1-4):207-220.
21. Tvergaard V. On fatigue crack growth in ductile materials by crack-tip blunting. *J Mech Phys Solids*. 2004;52(9):2149-2166.
22. Tvergaard V. Mesh sensitivity effects on fatigue crack growth by crack-tip blunting and re-sharpening. *Int J Solids Struct*. 2007;44(6):1891-1899.
23. Tvergaard V. Overload effects in fatigue crack growth by crack-tip blunting. *Int J Fatigue - INT J FATIGUE*. 2005;27(10-12): 1389-1397.
24. Kujawski D, Ellyin F. A fatigue crack propagation model. *Eng Fract Mech*. 1984;20(5-6):695-704.



25. Glinka G. A notch stress-strain analysis approach to fatigue crack growth. *Eng Fract Mech.* 1985;21(2):245-261.
26. Kujawski D, Ellyin F. A fatigue crack growth model with load ratio effects. *Eng Fract Mech.* 1987;28(4):367-378.
27. Chalant G, Remy L. Model of fatigue crack propagation by damage accumulation at the crack tip. *Eng Fract Mech - ENG Fract MECH.* 1983;18(5):939-952.
28. Davidson DL, Lankford J. Fatigue crack growth in metals and alloys: mechanisms and micromechanics. *Int Mater Rev.* 1992; 37(1):45-76.
29. de Castro JTP, Meggiolaro MA, de Oliveira Miranda AC. Fatigue crack growth predictions based on damage accumulation calculations ahead of the crack tip. *Comput Mater Sci.* 2009;46(1):115-123.
30. Schwalbe K-H. Comparison of several fatigue crack propagation laws with experimental results. *Eng Fract Mech.* 1974;6(2): 325-341.
31. Sérgio ER, Antunes FV, Borges MF, Neto DM. FCG modelling considering the combined effects of cyclic plastic deformation and growth of micro-voids. *Materials (Basel).* 2021;1-18.
32. Lemaitre J. Phenomenological aspects of damage. In: *A Course on Damage Mechanics.* Berlin, Heidelberg: Springer Berlin Heidelberg; 1996:1-37.
33. Tong J, Alshammrei S, Lin B, Wigger T, Marrow T. Fatigue crack closure: a myth or a misconception? *Fatigue Fract Eng Mater Struct.* 2019;42:2747-2763.
34. Lopez-Crespo P, Withers P, Yusof F, et al. Overload effects on fatigue crack-tip fields under plane stress conditions: surface and bulk analysis. *Fatigue Fract Eng Mater Struct.* 2013;36(1): 75-84.
35. Ravi P, Naragani D, Kenesei P, Park J-S, Sangid MD. Direct observations and characterization of crack closure during microstructurally small fatigue crack growth via in-situ high-energy X-ray characterization. *Acta Mater.* 2021;205: 116564.
36. Steuerer A, Santisteban J, Turski M, Withers P, Buslaps T. High-resolution strain mapping in bulk samples using full-profile analysis of energy-dispersive synchrotron X-ray diffraction data. *J Appl Cryst.* 2005;37(6):883-889.
37. Andersson M, Persson C, Melin S. Experimental and numerical investigation of crack closure measurements with electrical potential drop technique. *Int J Fatigue.* 2006;28(9):1059-1068.
38. Sunder R, Raut D, Jayaram V, Kumar P, Shastri V. Near-tip residual stress as an independent load interaction mechanism. *Int J Fatigue.* 2021;151:106364.
39. Antunes FV, Chegini AG, Branco R, Camas D. A numerical study of plasticity induced crack closure under plane strain conditions. *Int J Fatigue.* 2015;71:75-86.
40. Ritchie RO, Suresh S, Moss CM. Near-threshold fatigue crack growth in 2 1/4 Cr-1Mo pressure vessel steel in air and hydrogen. *J Eng Mater Technol.* 1980;102(3):293-299.
41. Suresh S, Ritchie RO. On the influence of fatigue underloads on cyclic crack growth at low stress intensities. *Mater Sci Eng A.* 1981;51(1):61-69.
42. Suresh S, Ritchie RO. A geometric model for fatigue crack closure induced by fracture surface roughness. *Metall Trans A.* 1982;13(9):1627-1631.
43. Alves JL, Revil-Baudard B, Cazacu O. Importance of the coupling between the sign of the mean stress and the third invariant on the rate of void growth and collapse in porous solids with a von Mises matrix. *Model Simul Mater Sci Eng.* 2014;22(2):025005.
44. Sérgio ER, Antunes FV, Borges MF, Neto DM. FCG modelling considering the combined effects of cyclic plastic deformation and growth of micro-voids. *Mater (Basel, Switzerland).* 2021; 14(15):4303.
45. Nahshon K, Hutchinson JW. Modification of the Gurson model for shear failure. *Eur J Mech - A/Solids.* 2008;27(1):1-17.
46. Malcher L, Andrade Pires FM, César De Sá JMA. An extended GTN model for ductile fracture under high and low stress triaxiality. *Int J Plast.* 2014;54:193-228.
47. Ying L, Wang D, Liu W, Wu Y, Hu P. On the numerical implementation of a shear modified GTN damage model and its application to small punch test. *Int J Mater Form.* 2018;11(4): 527-539.
48. Maia R, Branco R, Antunes FV, Oliveira MC, Kotousov A. Three-dimensional computational analysis of stress state transition in through-cracked plates. *Math Comput Sci.* 2016;10(3): 343-352.
49. Menezes LF, Teodosiu C. Three-dimensional numerical simulation of the deep-drawing process using solid finite elements. *J Mater Process Technol.* 2000;97(1-3):100-106.
50. Oliveira MC, Alves JL, Menezes LF. Algorithms and strategies for treatment of large deformation frictional contact in the numerical simulation of deep drawing process. *Arch Comput Methods Eng.* 2008;15(2):113-162.
51. Tinoco H, Cardona García C, Vojtek T, Hutar P. Finite element analysis of crack-tip opening displacement and plastic zones considering the cyclic material behaviour. *Procedia Eng.* 2019; 23:529-534.
52. Hosseini ZS, Dadfarnia M, Somerday BP, Sofronis P, Ritchie RO. On the theoretical modeling of fatigue crack growth. *J Mech Phys Solids.* 2018;121:341-362.
53. Tuegel EJ. *Measurements of Kinematic and Isotropic Hardening During Inelastic Cyclic Straining.* Netherlands: North-Holland; 1985.
54. Gurson AL. Continuum theory of ductile rupture by void nucleation and growth: part I—yield criteria and flow rules for porous ductile media. *J Eng Mater Technol.* 1977;99(1):2-15.
55. Tvergaard V. Influence of voids on shear band instabilities under plane strain conditions. *Int J Fract.* 1981;17(4):389-407.
56. Tvergaard V. On localization in ductile materials containing spherical voids. *Int J Fract.* 1982;18(4):237-252.
57. Nielsen KL. Predicting failure response of spot welded joints using recent extensions to the Gurson model. *Comput Mater Sci.* 2010;48(1):71-82.
58. Besson J. Continuum models of ductile fracture: a review. *Int J Damage Mech.* 2010;19(1):3-52.
59. Brito J. Ductile fracture prediction using a coupled damage model. 2018.
60. Malcher L. Continuum modelling and numerical simulation of damage for ductile materials. 2012.
61. Chu CC, Needleman A. Void nucleation effects in biaxially stretched sheets. *J Eng Mater Technol.* 1980;102(3):249-256.
62. Chen D, Li Y, Yang X, Jiang W, Guan L. Efficient parameters identification of a modified GTN model of ductile fracture using machine learning. *Eng Fract Mech.* 2021;245:107535.
63. Thomason PF. Ductile fracture of metals. 1990.

64. ASTM International. E647-00: standard test method for measurement of fatigue crack growth rates. *ASTM Int.* 2005;03: 1-45.
65. Antunes FV, Camas D, Correia L, Branco R. Finite element meshes for optimal modelling of plasticity induced crack closure. *Eng Fract Mech.* 2015;142:184-200.
66. Antunes FV, Borrego LFP, Costa JD, Ferreira JM. A numerical study of fatigue crack closure induced by plasticity. *Fatigue Fract Eng Mater Struct.* 2004;27:825-835.
67. Antunes FV, Sousa T, Branco R, Correia L. Effect of crack closure on non-linear crack tip parameters. *Int J Fatigue.* 2015;71: 53-63.
68. Borrego LP, Ferreira JM, Costa JM. Partial crack closure under block loading. *Int J Fatigue.* 2008;30(10-11):1787-1796.
69. Zhang ZL, Thaulow C, Ødegård J. A complete Gurson model approach for ductile fracture. *Eng Fract Mech.* 2000;67(2): 155-168.
70. Griffiths JR, Mogford IL, Richards CE. Influence of mean stress on fatigue-crack propagation in a ferritic weld metal. *Met Sci J.* 1971;5(1):150-154.

**How to cite this article:** Sérgio ER, Antunes FV, Neto DM. Fatigue crack growth modeling considering a hybrid propagation strategy. *Fatigue Fract Eng Mater Struct.* 2023;46(4):1613-1626. doi:[10.1111/ffe.13950](https://doi.org/10.1111/ffe.13950)